International Journal of Heat and Fluid Flow 102 (2023) 109162

Contents lists available at ScienceDirect

International Journal of Heat and Fluid Flow

journal homepage: www.elsevier.com/locate/ijhff

Logarithmic scaling of higher-order temperature moments in the atmospheric surface layer

Kelly Y. Huang [a,*], Matt K. Fu [b], Clayton P. Byers [c], Andrew D. Bragg [d], Gabriel G. Katul [d]

[a] Department of Civil and Environmental Engineering, University of Notre Dame, Notre Dame, 46556, IN, USA
[b] GALCIT, Caltech, Pasadena, 91125, CA, USA
[c] Department of Engineering, Trinity College, Hartford, 06109, CT, USA
[d] Department of Civil and Environmental Engineering, Duke University, Durham, 27708, IN, USA

ARTICLE INFO

Keywords:
Attached eddy hypothesis
Log law for high-order passive scalars
Random sweeping decorrelation hypothesis

ABSTRACT

A generalized logarithmic law for high-order moments of homogeneous passive scalars is proposed for turbulent boundary layers. This law is analogous to the generalized log law that has been proposed for high-order moments of the turbulent longitudinal velocity and is derived by combining the random sweeping decorrelation hypothesis with a spectral model informed by the attached eddy hypothesis. The proposed theory predicts that the high-order moments of passive scalar fluctuations within the inertial sublayer will vary logarithmically with wall-normal distance (z), and is evaluated using high frequency time-series measurements of temperature and streamwise velocity fluctuations obtained in the first meter of the atmospheric surface layer (ASL) under near-neutral thermal stratification. The logarithmic dependence with z within the inertial sublayer is observed in both the air temperature and velocity moments, with good agreement to the predictions from the proposed theory. Surprisingly, the proposed theory appears to be as, if not more, valid for transported passive scalars than for the longitudinal velocity.

1. Background

The ability to reproduce high-order streamwise velocity statistics $\overline{u'^{2p}}$ is relevant in evaluating subgrid models and post-processing of large eddy simulations (Stevens et al., 2014), and in the synthetic generation of turbulence where Morales et al. (2012) showed the need to characterize wind turbulence by high-order statistics beyond the mean and variance. Analogously, representing high-order statistics of the homogeneous scalar field is key to accurately modeling numerous atmospheric processes that depend on the temperature field (such as wildfires, fog, and other extreme weather events) or on the dispersion of passive scalars (such as the transport of pollutants and pollen).

The random sweeping decorrelation hypothesis (RSDH) is a kinematic model predicated on the assumption that small-scale eddies are swept by the larger, energetic eddies without any dynamic distortion (Tennekes, 1975). Hence, motion of the smaller scales, particularly in the inertial range, are excited by the kinetic energy of the large scales. Given that the statistics of the large scales are often reasonably described as being Gaussian, a consequence of this kinematic assumption is the tendency towards Gaussian statistics for any flow quantities that are directly impacted by this sweeping effect. The RSDH therefore leads to significant simplifications in modeling since Gaussian random variables have known analytical expressions for their probability distribution functions and associated statistics. In stationary and planar-homogeneous turbulent boundary layer flow at high Reynolds number (Re), this Gaussian behavior provides a convenient ansatz upon which generalized statistical predictions can be formed.

By assuming a Gaussian probability distribution for the streamwise velocity fluctuations (u') and that the turbulent eddies are non-interacting, Meneveau and Marusic (2013) were able to develop a generalized logarithmic law for the high-order statistics of u' in the inertial sublayer given by

$$\left(\overline{u'^{2p}}^{+}\right)^{1/p} = B_p - A_p \ln\left(\frac{z}{\delta}\right), \tag{1}$$

where $p \geq 1$ is the moment order, B_p is a flow-dependent constant, $A_p = A_1\,[(2p-1)!!]^{1/p}$, $A_1 \approx 1.25$ is the Townsend–Perry constant (see Smits et al., 2011; Marusic et al., 2013; Meneveau and Marusic, 2013), !! is the double factorial, z is the wall-normal distance, δ is an outer length scale such as the boundary layer height, and the + superscript indicates normalization by the friction velocity u_*. Following convention, w' and u' specify the wall-normal velocity and streamwise velocity, respectively, and primed quantities are turbulent fluctuations from the mean state that is indicated by overline. For stationary and planar

* Corresponding author.
E-mail address: yhuang28@nd.edu (K.Y. Huang).

https://doi.org/10.1016/j.ijheatfluidflow.2023.109162
Received 9 December 2022; Received in revised form 19 April 2023; Accepted 8 May 2023
Available online 20 May 2023
0142-727X/© 2023 Elsevier Inc. All rights reserved.

homogeneous high Re flow in the absence of subsidence or mean pressure gradients, the friction velocity u_* is approximately equal to $\sqrt{-\overline{u'w'}}$ which is independent of z in the constant stress layer.

The scaling law of Eq. (1) can be recovered through simpler arguments that take advantage of two hypotheses developed independently for different ranges of scales: (i) the RSDH describing the behavior of small-scale motion, and (ii) the attached eddy hypothesis describing the wall effects on large-scale motion. As shown here, the RSDH can be used to generalize the behavior of high-order spectra and the consequences of the attached eddy model can be used to describe scaling laws of the low-wavenumber properties of u' (Katul et al., 2016). In arriving at Eq. (1), high-order spectra were related via RSDH to a model spectrum for u' characterized by a k^{-1} scaling regime of wavenumber k at large scales (i.e., attached eddies) and $k^{-5/3}$ for inertial scales (i.e., detached eddies) up to the Kolmogorov micro-scale. Integration of this model spectrum and its combination with RSDH then recovered Eq. (1) and linked A_p and B_p explicitly to the Kolmogorov constant and Re for Gaussian statistics.

While RSDH has been investigated extensively in terms of the turbulent velocity, particularly u', significantly less attention has been paid to the behavior of passive scalar fields, such as temperature in near-neutral stratification. Previous numerical studies have indicated that in isotropic turbulence, passive scalar fields adhere to the RSDH as well as, if not better than, the velocity field (Yeung and Sawford, 2002) with near-Gaussian probability distributions (Overholt and Pope, 1996). Further, numerous studies have empirically established the statistical similarities between streamwise velocity and passive scalar fluctuations in wall-bounded turbulence, beginning with the predictions of Reynolds analogy and more rigorous derivations of logarithmic behavior of the mean velocity and scalar profiles consistent with classical overlap arguments (Kader, 1981; Marusic et al., 2013). In particular, while Kader (1981) found the mean temperature profile follows a logarithmic law in turbulent pipes, channels, and boundary layers, the turbulent Prandtl number was slightly less than unity, indicating a departure from Reynolds analogy. This departure has been corroborated through multiple experiments and numerical simulations through the decades, where it appears that the turbulent Prandtl number will approach 0.85 in the logarithmic region in air (Kays, 1994; Wu and Moin, 2010; Castillo and Hussain, 2017). Nonetheless, the mean and variance profiles of the temperature field in a zero-pressure-gradient boundary layer follow logarithmic profiles, independent of any assumption of Reynolds analogy.

The similarity of these fluctuating quantities has become increasingly evident with the advent of direct numerical simulations (DNS) of turbulent channel flow, beginning with Kim and Moin (1987) who found correlation coefficients between the streamwise velocity and scalar fluctuations up to 0.95, at $Re_\tau = \delta u_*/\nu = 180$, where δ, here, is the channel half-height. Recent simulations at higher Re_τ up to 4088 for $Pr = 0.7$–1 by Pirozzoli et al. (2016) similarly revealed that the streamwise velocity variance and passive scalar variance continue to exhibit qualitatively similar wall-normal profiles. These observations were formalized by Yang and Abkar (2018), who proposed a model by which passive scalars fields were interpreted through the established theoretical frameworks based on Townsend's attached eddy hypothesis (Townsend, 1976) for streamwise velocity fluctuations. The treatment of the passive scalar field through this superposition model of wall-attached eddies explicitly recovers a k^{-1} scaling behavior for wavenumbers corresponding to the attached eddies. Through the use of their model and a large eddy simulation, Yang and Abkar (2018) found logarithmic scaling of the passive scalar moments and a scalar/velocity correlation coefficient that was less than 1 and approaches 0.85 for large Re, corroborating the prior work of Subramanian and Antonia (1981), Kim and Moin (1987), Kasagi et al. (1992), Wu and Moin (2010). These treatments highlight the similarities between the velocity and passive scalar field, even when Reynolds analogy does not hold, mainly through the mechanism of the kinematics of scalars being carried by the momentum. However, care must be taken in the theoretical development for passive scalar fields. The absence of the pressure gradient from the dynamical equations for the mean and fluctuating temperature fields results in a more effective mixing of momentum rather than heat (Guezennec et al., 1990). This means that temperature as a passive scalar is not necessarily an effective marker of the vortical structure and therefore departures between theoretical treatments of temperature and velocity must be accounted for, especially as the logarithmic behavior of the temperature field is more sensitive to deviations from ideal zero-pressure-gradient conditions (Bradshaw and Huang, 1995). Recently, Cheng et al. (2021) investigated unstably stratified atmospheric boundary layers and how the buoyancy affects the statistics of passive scalars, determining that logarithmic behavior persisted in the mean, but with a modified slope. Their findings emphasize the need to account for non-universal behavior with the presence of thermal stratification, whereas many previous passive scalar studies assume a universal logarithmic behavior (Kader and Yaglom, 1972; Kader, 1981; Kasagi et al., 1992). In finding analogies between velocity fluctuations and temperature fluctuations, the assumption of a passive scalar field is critical. Nevertheless, even in this case, small-scale statistics of passive scalar fields can differ profoundly from those of the velocity field (Warhaft, 2000), and modeling approximations that work well for the velocity field, e.g. the assumption of small-scale isotropy, may not work well for the scalar field (Sreenivasan, 1991; Warhaft, 2000).

Here, a new theory based on RSDH and informed by the similarity between temperature and streamwise momentum is developed for the behavior of passive scalar moments in the inertial sublayer and tested at very high Re not attainable in laboratory settings or direct numerical simulations. The predicted logarithmic behavior of the high-order passive scalar moments is found to be in agreement with highly resolved measurements of temperature obtained in the atmospheric surface layer under near-neutral conditions. Further, the deviations between the temperature statistics and their corresponding theoretical predictions are found to be comparable to and, in some instances, smaller than those found for the collocated streamwise velocity.

2. Theory

Decades of studies have found a k^{-1} scaling of temperature spectra in the atmospheric surface layer with good agreement in multiple stability conditions (Pond et al., 1966; Katul et al., 1995; Li et al., 2016; Yang and Abkar, 2018) in addition to the measurements presented here. Combining these results with the $k^{-5/3}$ inertial range behavior through the method of Katul et al. (2016) and Huang and Katul (2022) allows for the theoretical development of a logarithmic law in the high-order even moments of the temperature variance given by

$$\left(\overline{\theta'^{2p}}^{+}\right)^{1/p} = B_{p,\theta'} - A_{p,\theta'} \ln\left(\frac{z}{\delta}\right), \tag{2}$$

where θ' is the virtual potential temperature fluctuations, $B_{p,\theta'}$ is a flow-dependent offset, $A_{p,\theta'}$ is the slope, analogous to the Townsend-Perry constant in Eq. (1), and the + superscript again indicates normalization by the inner temperature scale θ_* given by the scalar wall flux and friction velocity, which in the constant stress layer may be approximated as $\theta_* \approx -\overline{w'\theta'}/u_*$.

Eq. (2) is derived by considering the time series for the passive scalar fluctuation, θ'. The integral of the p^{th}-order spectrum, $E^{(p)}_{\theta'}(k)$, is related to statistical moments of θ' through

$$\overline{(\theta'^p - \overline{\theta'^p})^2} = \overline{\theta'^{2p}} - \overline{\theta'^p}^2 = \int_0^{+\infty} E^{(p)}_{\theta'}(k)\, dk. \tag{3}$$

Under the assumptions of RSDH, the probability distribution function (PDF) of the time series is taken to be normally distributed, allowing the higher-order statistical moments and spectra to be expressed analytically as a function of the second ($p = 1$) moment resulting in

$$E^{(p)}_{\theta'}(k) = \alpha(p)\overline{\theta'^2}^{p-1} E_{\theta'}(k), \tag{4}$$

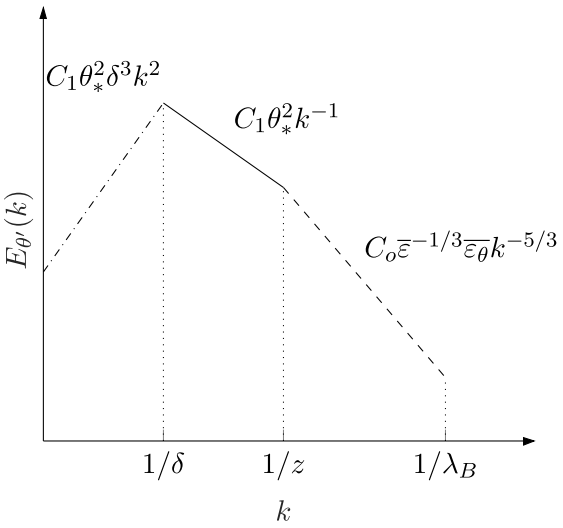

Fig. 1. Illustration of an idealized piecewise temperature spectrum and its scaling regimes as a function of wavenumber k. The k^2 behavior (analogous to the Saffman spectrum) is the minimum required for $dE_\theta/dk \to 0$ as $k \to 0$. For analytical tractability, the Kolmogorov $k^{-5/3}$ inertial scaling is extended to the Batchelor scale λ_B with a cutoff compensating for the energy contribution not resolved here by the expected exponential decay due to molecular effects.

where

$$\alpha(p) = p^2 \times 1 \times 3 \times 5 \times \cdots \times (2p-3)$$

is a consequence of Gaussian statistics for $p > 1$.

The high-order moments for temperature

$$\overline{\theta'^{2p}} = \int_0^\infty E_{\theta'}^{(p)}(k)\,dk + \overline{\theta'^p}^2$$

are now interpreted with the RSDH (see Eq. (4)) to yield

$$\overline{\theta'^{2p}} = \alpha(p)\left[\overline{\theta'^2}\right]^{p-1}\int_0^\infty E_{\theta'}(k)\,dk + \overline{\theta'^p}^2. \tag{5}$$

It can be shown for Gaussian statistics that the $\overline{\theta'^p}^2$ term is zero for odd p and diminishes rapidly for even p so that its contribution is only significant for $p = 2$ with a value of $(3/2)\overline{\theta'^{2p}}$.

To arrive at an analytic expression, an idealized shape for $E_{\theta'}(k)$ is prescribed and shown in Fig. 1 based on Huang and Katul (2022) and given by the piecewise function

$$E_{\theta'}(k) = \begin{cases} C_1\theta_*^2\delta^3k^2 & \text{if } k \in [0, \delta^{-1}] \\ C_1\theta_*^2k^{-1} & \text{if } k \in [\delta^{-1}, z^{-1}] \\ C_\theta\overline{\varepsilon}^{-1/3}\overline{\varepsilon_\theta}k^{-5/3} & \text{if } k \in [z^{-1}, \lambda_B^{-1}] \\ 0 & \text{if } k > \lambda_B^{-1}, \end{cases} \tag{6}$$

where $\lambda_B = Sc_m^{-1/2}\eta$ is the Batchelor scale, close to the Kolmogorov micro-scale η in near-neutral atmospheric flows because the molecular Schmidt number (Sc) is close to unity for temperature and many other scalars (and Eq. (6) already assumes $Sc = O(1)$ when prescribing the spectrum scaling for $k \in [z^{-1}, \lambda_B^{-1}]$). Here, we have adopted the canonical scaling laws in the high wavenumber regime based on Kolmogorov–Obukhov–Corrsin (KOC) theory (Kolmogorov, 1941; Obukhov, 1949; Corrsin, 1951) for isotropic turbulence. For the applications of interest such as the atmospheric surface layer, shear effects on spectral exponents in the inertial subrange can be assumed to be minimal (Tennekes and Lumley, 1972). However, in locations or applications where anisotropy effects may not be negligible, alternative scaling may need to be adopted to account for such effects, e.g., see the $-4/3$ scaling proposed by Lohse (1994). The low wavenumber behavior (i.e., $k \le \delta^{-1}$) is modeled after Saffman, 1967 to ensure the energy contribution in the very large scales is not singular as $k \to 0$. This choice is a deviation from the functional form proposed by Katul et al. (2016), who applied a constant value in this region. Assuming that production of turbulent kinetic energy and temperature variance are each balanced by their respective dissipation within the inertial sublayer (i.e., $\overline{\varepsilon} = u_*^3/\kappa z$ and $\overline{\varepsilon}_\theta = u_*\theta_*^2/\kappa z$, and $\kappa \approx 0.41$), the spectral model in Eq. (6) can be integrated, giving

$$\int_0^\infty E_{\theta'}(k)\,dk = \overline{\theta'^2} = \int_0^{1/\delta} C_1\theta_*^2\delta^3k^2\,dk + \int_{1/\delta}^{1/z} C_1\theta_*^2k^{-1}\,dk + \int_{1/z}^{1/\lambda_B} C_\theta\overline{\varepsilon_\theta}^{-2/3}k^{-5/3}\,dk,$$

allowing the temperature variance to ultimately be expressed as

$$\frac{\overline{\theta'^2}}{\theta_*^2} \equiv \overline{\theta'^2}^+ = C_1\left[\frac{11}{6} - \frac{3}{2}\left(\frac{\lambda_B}{z}\right)^{2/3}\right] - C_1\ln\left(\frac{z}{\delta}\right). \tag{7}$$

Eq. (7) recovers the logarithmic form proposed in Eq. (2) where

$$A_{1,\theta'} = C_1$$

and

$$B_{1,\theta'} = C_1\left[\frac{11}{6} - \frac{3}{2}\left(\frac{\lambda_B}{z}\right)^{2/3}\right].$$

Note the value of C_θ is related to C_1 through matching the piecewise function at $k = 1/z$. Eq. (5) can then be written as

$$\overline{\theta'^{2p}} = \alpha(p)\left[\overline{\theta'^2}\right]^{p-1}\theta_*^2\left[B_{1,\theta'} - A_{1,\theta'}\ln\left(\frac{z}{\delta}\right)\right]. \tag{8}$$

Finally, substituting

$$\overline{\theta'^2} = \theta_*^2\left[B_{1,\theta'} - A_{1,\theta'}\ln\left(\frac{z}{\delta}\right)\right],$$

normalizing by θ_*^{2p}, and raising to a power of $1/p$ provides the sought result

$$(\overline{\theta'^{2p}}^+)^{1/p} = \alpha(p)^{1/p}\left[B_{1,\theta'} - A_{1,\theta'}\ln\left(\frac{z}{\delta}\right)\right]. \tag{9}$$

This expression has the same form as Eq. (2) with

$$A_{p,\theta'} = \alpha(p)^{1/p}A_{1,\theta'}$$

and

$$B_{p,\theta'} = \alpha(p)^{1/p}B_{1,\theta'}.$$

3. Experimental methodology & data

As part of the Idealized horizontal Planar Array study for Quantifying Surface heterogeneity (IPAQS) (Morrison et al., 2021) that took place at the Surface Layer Turbulence and Environmental Science Test (SLTEST) facility in the western deserts of Utah, USA, measurements of longitudinal velocity and temperature were acquired at $z = 0.0625$, 0.125, 0.25, 0.5, and 1.0 m above the ground during a three-day intensive sampling period (18–20 June 2018). Due to sensor breakage, temperature measurements at $z = 0.5$ m are not represented in the analysis below. The SLTEST facility is a unique field site with near-canonical boundary conditions (its aerodynamic roughness ranges from sub-millimeter to less than 6 mm) and predictable wind patterns, making it an ideal location for probing high Re turbulent boundary layer flows (Klewicki et al., 1998; Metzger and Klewicki, 2001). The equivalent sand grain roughness for these measurements was estimated to be 2.5 mm using the relation for a zero-pressure-gradient neutral boundary layer (Huang et al., 2021a), meaning the lowest station height corresponds to 25 times that of the equivalent sand grain roughness.

Nano-scale thermal anemometry probes (NSTAPs) operated in constant-current anemometry mode and their cold-wire variants

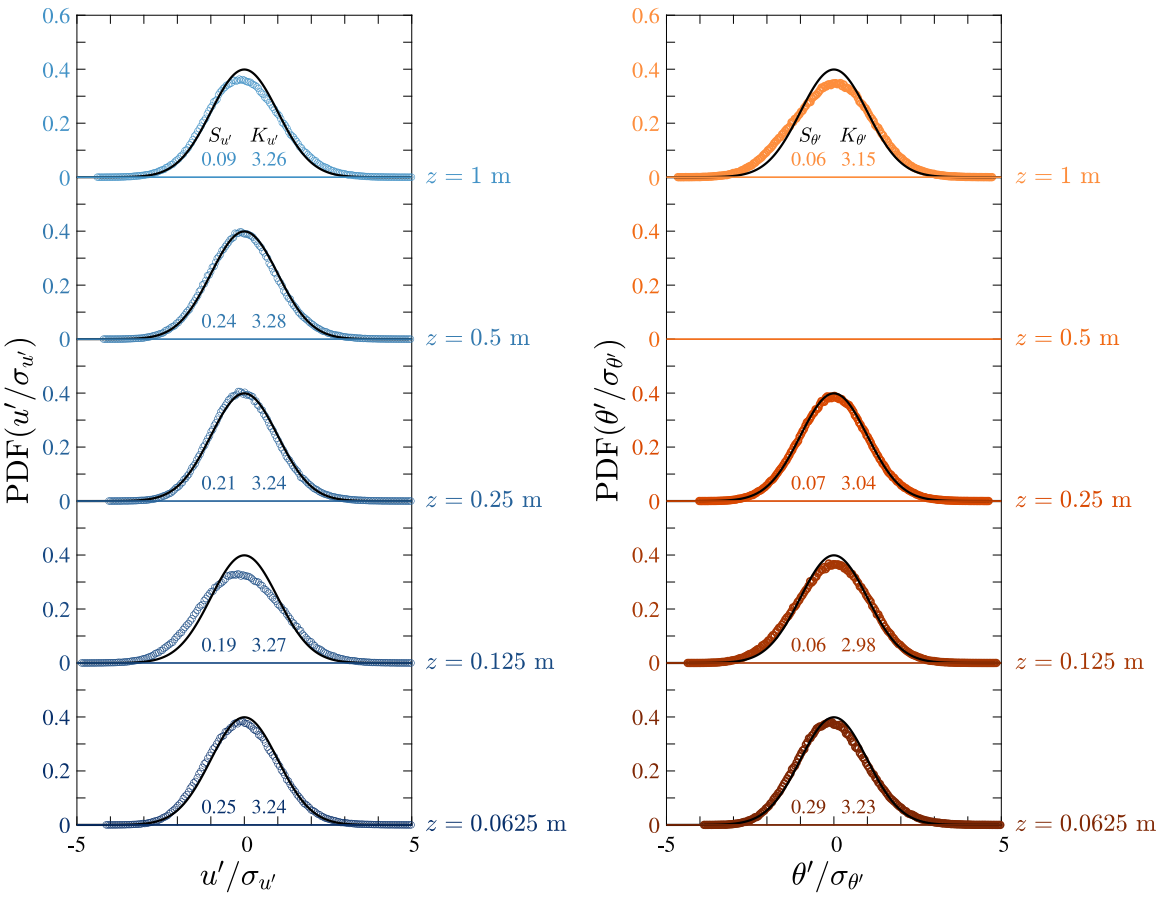

Fig. 2. Measured probability density functions (open symbols) of the velocity (left) and temperature (right) fluctuations at $z = 1$ m, $z = 0.5$ m, $z = 0.25$ m, $z = 0.125$ m, and $z = 0.0625$ m. The solid black line indicates a Gaussian distribution. (For interpretation of the references to color in this figure legend, the reader is referred to the web version of this article.)

Table 1
Mean flow properties relative to the triaxial sonic anemometer positioned at $z = 2$ m for the 30-min periods analyzed (local time LT = UTC + 6 h) on 21/06/2018. The boundary layer height δ was estimated to be 60 m (Huang et al., 2021b), and R_f was estimated using both the sonic anemometer data and the mean velocity profile given by the NSTAPs evaluated at $z = 2$ m.

LT	$\overline{u}$ (m s^{-1})	u_* (m s^{-1})	$\overline{w'\theta'_v}$ (K m s^{-1})	ζ	R_f
2000	7.55	0.28	−0.017	0.025	0.014
2030	6.56	0.22	−0.018	0.053	0.040
2200	6.60	0.24	−0.024	0.056	0.035
2230	7.34	0.29	−0.029	0.038	0.016

(TNSTAPs) were used to capture velocity and temperature measurements, respectively, at each height with a sampling frequency of 100 Hz. The sensing elements of these nano-scale sensors are platinum wire ribbons 2 μm in width, 100 nm in thickness, 60 μm in length for the NSTAP and 200 μm in length for the TNSTAP. The size of these sensors provides high spatial resolution with minimized end-conduction effects and temporal filtering (Hultmark et al., 2011; Arwatz et al., 2015). Relevant stresses and heat fluxes are calculated from data acquired by a nearby triaxial sonic anemometer (Campbell Scientific CSAT3) at approximately 10 m west of the measurement tower at $z = 2$ m. The approximate number of large eddy turnovers ranges from 196 to 1180, depending on the particular calculation. Note this is likely an underestimate, as the mean convective velocity $\bar{u}$ is calculated at the 2 m height and not the freestream velocity. Further details on the different estimates of eddy turnovers can be found in the appendix. Details regarding the experimental set-up and calibration procedure can be found elsewhere (Huang et al., 2021a).

Trends associated with the varying freestream velocity were subtracted from the raw time series (Hutchins et al., 2012). Four 30-min records are examined in the current study and summarized in Table 1 after the following data qualifications:

1. The incoming wind direction aligned with the sensors (with pitch angle ±10° in accordance with the sensitivity of the NSTAP (Fan et al., 2015)), as verified by the sonic anemometer.
2. Near-neutral stability was reached, with both the Monin–Obukhov stability parameter $|\zeta| = |z/L| \approx 0$ and the flux Richardson number $R_f \approx 0$. The Obukhov length L is defined as

$$L = -\frac{u_*^3}{\kappa\left(g/\overline{\theta_v}\right)\overline{w'\theta'_v}}, \tag{10}$$

   where g is the acceleration due to gravity, and $\overline{\theta_v}$ is the mean virtual potential temperature. The flux Richardson number R_f is defined as

$$R_f = \frac{(g/\overline{\theta_v})\overline{w'\theta'_v}}{\overline{w'u'}(d\overline{u}/dz)}. \tag{11}$$

3. Stationarity of $\overline{u}$ and turbulence intensity $u'/\overline{u}$ were observed, as assessed by the reverse arrangement test and the runs test with a 95% confidence interval (Bendat and Piersol, 2011).

The four runs satisfying these conditions were near midnight (local time) when the stable boundary layer depth has equilibrated to its near-neutral value. Taylor's hypothesis was used to convert temporal differences in the velocity and temperature signals to spatial differences in the streamwise direction.

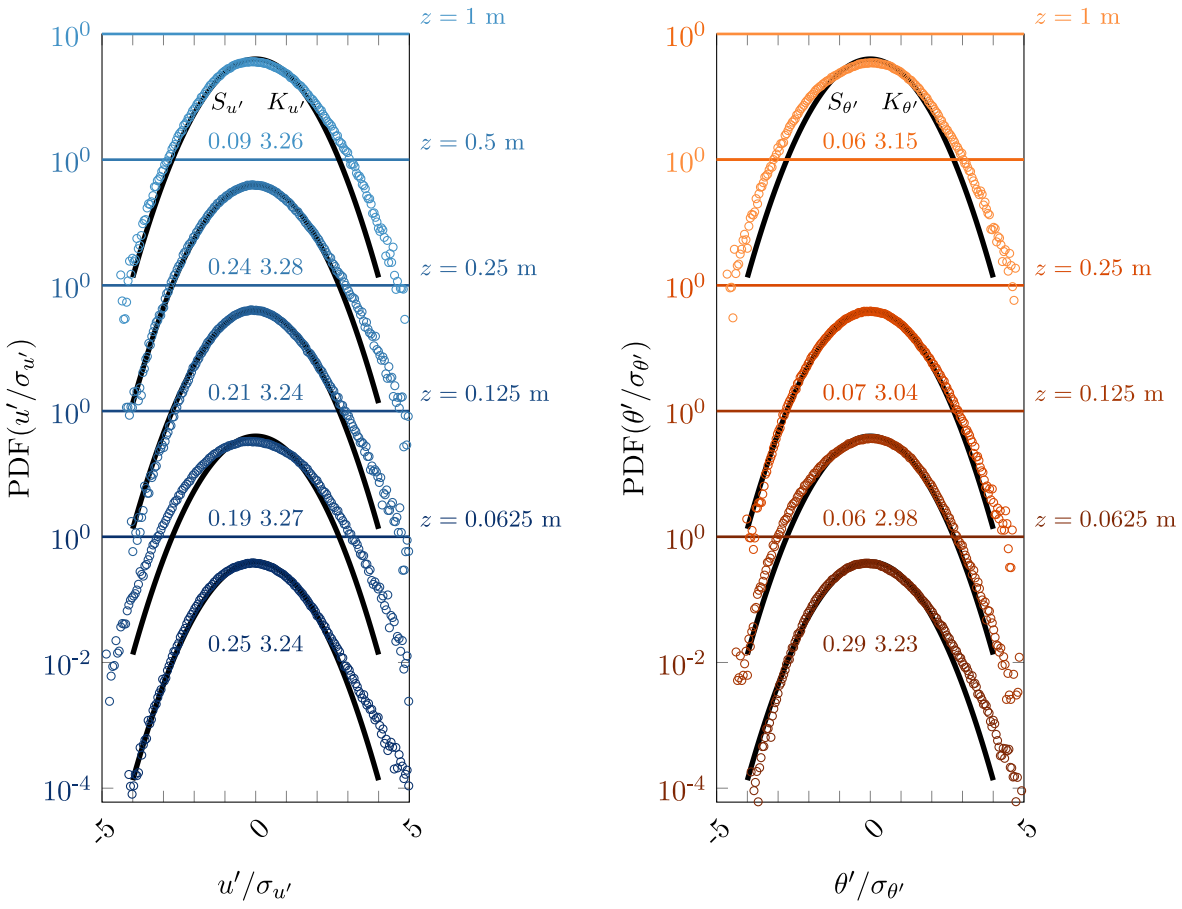

Fig. 3. Same as Fig. 2 but in semi-log space to highlight deviation in the tails.

Table 2
Kolmogorov–Smirnov statistics.

z (m)	K–S statistics	
	u'	θ'
0.0625	0.017	0.021
0.125	0.014	0.006
0.25	0.015	0.005
0.5	0.018	–
1.0	0.011	0.010

4. Results

Before evaluating the model predictions, this dataset can be used to first assess the validity of the key assumptions underpinning the proposed model. These are (i) the tendency towards Gaussian statistics, (ii) the existence of inertial range behavior, and (iii) spectral behavior consistent with the attached eddy model.

The Gaussian behavior of the velocity and temperature fluctuations can be assessed using the PDFs of the measurements. The PDFs for each quantity are shown in Fig. 2 at each measurement station height. The PDFs are normalized by their standard deviation $\sigma_{u'}$ and $\sigma_{\theta'}$, respectively and their skewness $S_{u'}$ and $S_{\theta'}$ and kurtosis $K_{u'}$ and $K_{\theta'}$ are shown. The same information is presented in semilog-space in Fig. 3 to highlight deviations in the tails. The bulk of both temperature and velocity statistics exhibit near-Gaussian behavior, with the most evident deviations being super-Gaussian in the positive tail.

The deviations of these velocity and temperature PDFs from Gaussian behavior are highlighted in Fig. 4 for each measurement height where collocated measurements were obtained. Each of the PDFs from Fig. 3 is normalized by the Gaussian distribution such that deviations from Gaussian behavior are indicated in proportion to unity. In addition, Kolmogorov–Smirnov (K–S) test statistics are presented in Table 2 to highlight maximum deviations from the normal cumulative distribution function. It can be seen that the scalar and velocity PDFs exhibit similar behavior for $-2 < \theta'/\sigma_{\theta'}$ (or $u'/\sigma_{u'}$) < 2. For $z = 0.125$ m and $z = 0.25$ m, the scalar PDFs are found to be within $\pm 10\%$ of a Gaussian distribution for a wider region, and exhibit smaller deviations from Gaussian behavior in the tails compared to their velocity counterparts. Though the exact behavior and statistics differ with station height, the tendency for the temperature fluctuations towards similar Gaussian behavior relative to the collocated velocity is a consistent feature across all z. These findings agree with prior sonic anemometry measurements collected above a dry lake bed (Chu et al., 1996).

The super-Gaussian behavior in the positive tails differs from the observations of Meneveau and Marusic (2013) and Samie et al. (2018) who observed sub-Gaussian behavior for boundary layer measurements up to $Re_\tau = 20{,}000$, and is potentially indicative of effects stemming from the roughness sublayer (Heisel et al., 2020). Recent studies such as Marusic et al. (2013) and Wei et al. (2005) suggest that the extent of the buffer layer could be Reynolds number dependent, extending up to $z^+ \approx 3(\delta u_*/\nu)^{1/2} \approx 3 \times 10^3$, with ν being kinematic viscosity, even in smooth-wall conditions. This criteria places the lowest two measurement heights within the buffer region where sweeps tend to dominate (Heisel et al., 2020).

The existence of an inertial subrange can be substantiated by assessing whether the lower order statistics of the measurements, such as mean and variance, exhibit a canonical logarithmic behavior. Following Vallikivi et al. (2015) who found logarithmic behavior above

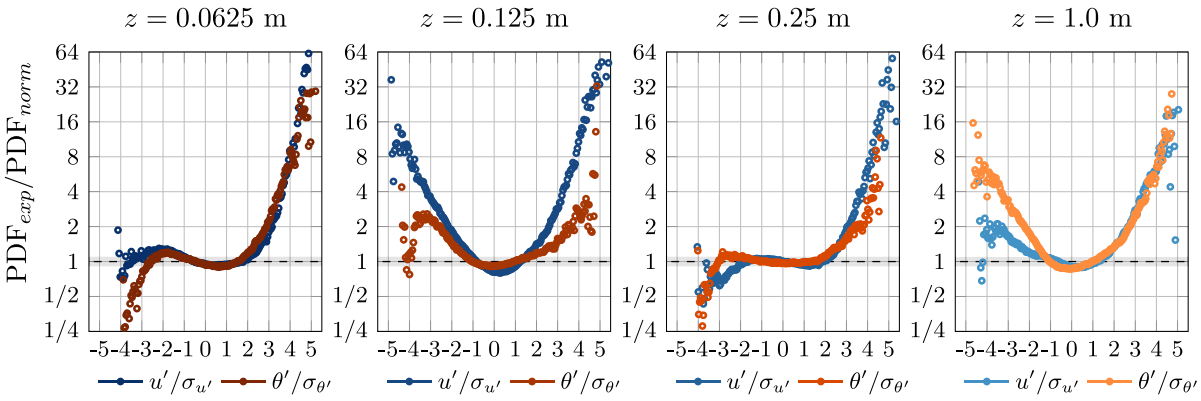

Fig. 4. Deviations of measured PDFs from Gaussian behavior. PDFs of measured velocity (blue) and temperature (orange) are normalized by a Gaussian distribution given by $\mathrm{PDF}_{norm} = \exp\left(-x^2/2\right)/\sqrt{2\pi}$, where $x = u'/\sigma_{u'}, \theta'/\sigma_{\theta'}$. Dashed black line (—) at unity indicates Gaussian behavior with a gray band showing the region of ±10% deviation. Values less than and greater than 1 indicate sub-Gaussian and super-Gaussian behavior, respectively. (For interpretation of the references to color in this figure legend, the reader is referred to the web version of this article.)

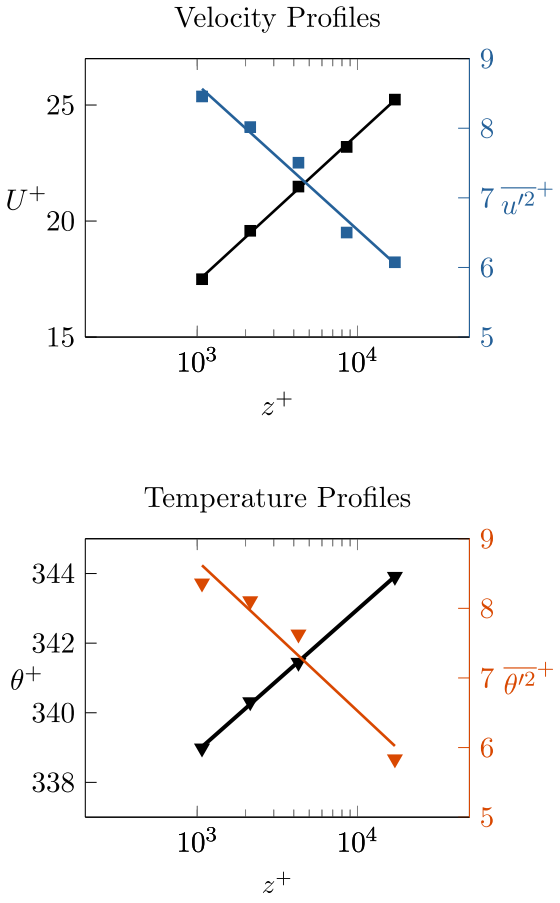

Fig. 5. Mean and variance profiles for velocity (top) and temperature (bottom) as a function of wall distance and normalized by inner units. Mean quantities U^+ and θ^+ are presented in black symbols with lines of best fit $U^+ = 2.75\log(z^+) - 1.6$ and $\theta^+ = 1.77\log(z^+) + 326.7$ given in black solid lines. Variances for velocity $\overline{u'^2}^+$ and temperature $\overline{\theta'^2}^+$ are denoted in blue and orange, respectively, with lines of best fit $\overline{u'^2}^+ = 14.9 - 0.91\log(z^+)$ and $\overline{\theta'^2}^+ = 15.1 - 0.94\log(z^+)$ denoted in solid lines. (For interpretation of the references to color in this figure legend, the reader is referred to the web version of this article.)

$z^+ = zu_*/\nu > 400$, the lowest measurement station to the ground at $z^+ \approx 850$ should be well within the log-layer. This assumption is further supported by the mean and variance profiles for the velocity and temperature shown in Fig. 5, where logarithmic behavior is found in the region $10^3 < z^+ < 10^4$. Here, A_1 and $A_{1,\theta'}$ are estimated as 0.91 and 0.94, respectively, by a least squares fitting of the data to Eq. (1). This value for the velocity compares reasonably well the $A_1 \approx 1.25$ found by Meneveau and Marusic (2013).

Table 3
Percentage of area represented by the three regions of the model spectrum for each measurement station.

z (m)	k^2 (% contribution)	k^{-1}	$k^{-5/3}$
0.0625	3.9	79.6	16.5
0.125	4.2	77.6	18.2
0.25	4.6	75.3	20.1
1.0	5.6	69.3	25.1

Finally, the streamwise wavenumber spectra of the velocity and temperature fluctuations can be compared to the idealized model, each of which are shown in Fig. 6. In both quantities, distinct k^{-1} and $k^{-5/3}$ scaling regions are identified, consistent with the assumptions of the simplified model. However, due to the lack of convergence and stationarity of the flow, no data are available in the low wavenumber region where the k^2 scaling is assumed. The expected area under the modeled k^2 region is identically equal to $\frac{1}{3}C_1$ in normalized variables. Compared to the integrated normalized spectrum of Fig. 6 for each case, this comes out to between 3.90% and 5.63% of the total integrated area, whereas the k^{-1} region represents 69.3% to 79.6% and the $k^{-5/3}$ region represents 16.5% to 25.1%, as seen in Table 3. As the contribution from the k^2 region only affects the offset $B_{1,\theta'}$ in Eq. (9), and the relative contribution remains small, the overall agreement between the model spectrum and the dataset is acceptable for the purposes here. Had a constant value for the spectrum been used such as Katul et al. (2016) or Huang and Katul (2022), the area would have been significantly higher, overemphasizing the contribution from these wavenumbers and increasing the offset $B_{p,\theta'}$.

Given the strength of the underlying assumptions, the predictive capability of the proposed RSDH model in capturing the behavior of the high-order moments can now be assessed. Because the temperature exhibits a distribution that more closely follows Gaussian behavior, the RSDH predictions for high-moments should hold for $(\overline{\theta'^{2p}}^+)^{1/p}$. A comparison between the high-order moments and the RSHD predictions can be seen in Fig. 7 for both the velocity and temperature measurements. In each case, the slope and offset of the $p = 1$ statistics (i.e., the variances) are determined from integration of the spectral RSDH models

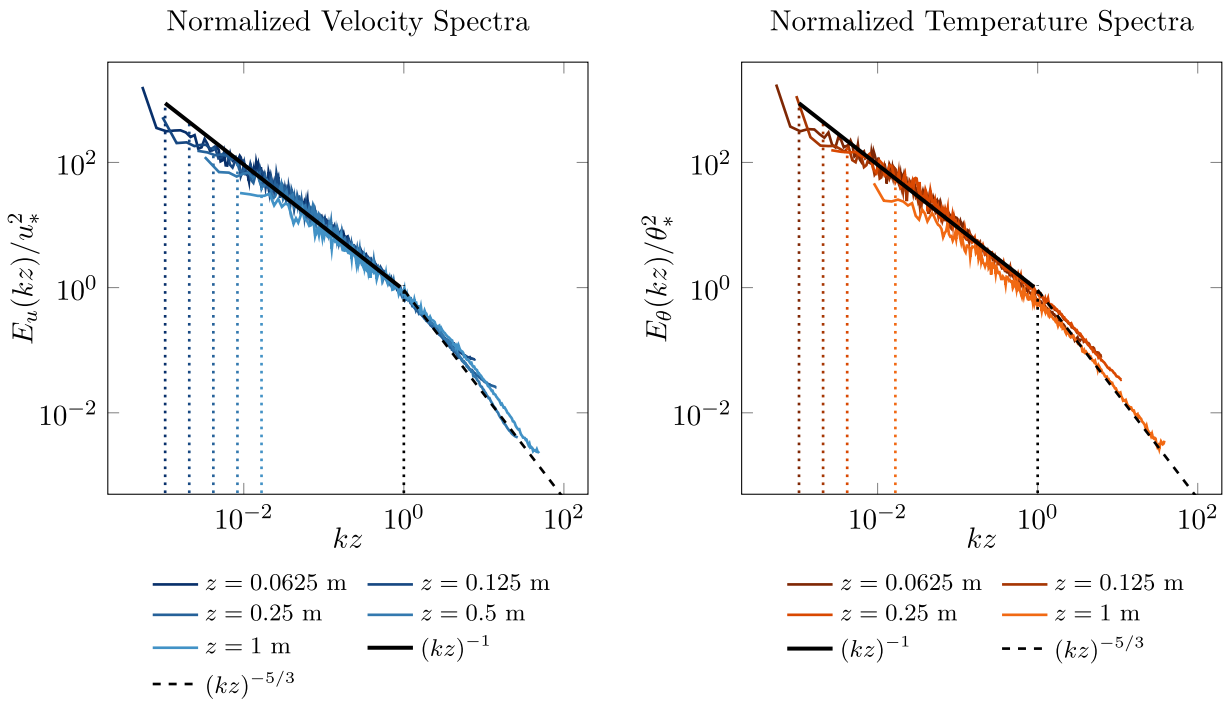

Fig. 6. Normalized spectra of the longitudinal velocity ($E_{u'}(kz)/u_*^2$) and temperature ($E_{\theta'}(kz)/\theta_*^2$) are computed using the frozen turbulence hypothesis (Taylor, 1938) and shown as a function of normalized wavenumber kz in the left and right plots, respectively. Different shades of blue and orange indicate the respective spectra for velocity and temperature at the different measurement stations with lighter shades corresponding to distances further from the ground. For each quantity, there is a clear break point between the k^{-1} (——) and the $k^{-5/3}$ (– –) scaling regimes as indicated by the black vertical dotted line (···) at $k = 1/z$. The $k = 1/\delta$ cutoff between the k^2 and the k^{-1} scaling regimes are also shown for each measurement height and denoted by their respective colors noted in the legend below each plot. (For interpretation of the references to color in this figure legend, the reader is referred to the web version of this article.)

given by Katul et al. (2016) and the present study (see Eq. (7)) rather than fitting a regression to the variance profiles. Similarly, the RSDH predictions for the high-order moments are determined from the $p = 1$ case through Eq. (9) that can be applied analogously to both velocity and temperature.

Fig. 7 shows that for both temperature and velocity, there appears to be good agreement between the measurements and their respective spectral RSDH models. In each case, the model is well within the statistical uncertainty related to limited convergence, with the exception of the $p = 2$ case, partially due to the additive $(3/2)\overline{\theta'^{2p}}$ contribution as noted in the theory section of the manuscript. Further, it is difficult to discern any significant differences in the performance of the model between the two quantities.

However, the differences between the temperature and velocity statistics become more apparent in Fig. 8, which directly compares the slopes (A_p and $A_{p,\theta'}$) and offsets (B_p and $B_{p,\theta'}$) obtained from the measurements and RSDH model. There, the slope and offset values from the RSDH predictions are extracted from the lines shown in Fig. 7 and plotted in the upper and lower plots of Fig. 8, respectively, as a function of moment order p. These predictions are compared with experimental values obtained from a linear regression of the high-order moments with the logarithmic wall distance, with error bars representing a 95% confidence interval on these calculated values. The performance of the RSDH model is comparable for velocity and temperature for $p \leq 3$, with the greatest deviation appearing at $p = 4$. The temperature prediction all falls within the 95% confidence interval for each value, while velocity has a small deviation for the even moments, albeit with narrower confidence intervals. This discrepancy is expected to widen for progressively larger values of p due to the increasing prevalence of the distribution tails to the higher-order moments; however, such high-order moments are not analyzed here due to limited convergence of these statistics in the present dataset.

5. Discussion

A logarithmic behavior of the high-order passive scalar moments in a homogeneous field (which differs from the scalar structure in a plume) is developed for the inertial sublayer based on RSDH and the similarity between temperature and streamwise momentum. The proposed theory is tested using a unique high-resolution atmospheric dataset with collocated streamwise velocity and temperature measurements under near-neutral stability conditions. The theory was able to reasonably predict both the slope $A_{p,\theta'}$ and the offset $B_{p,\theta'}$ up to moment order $p = 4$. A discussion now follows of the study limitations and model assumptions regarding (i) the experimental setup, (ii) Gaussian statistics, (iii) the extension to higher-order spectra under RSDH (Eq. (4)), and (iv) the logarithmic law for the mean temperature and the existence of the k^{-1} region in the first order temperature spectra.

While field experiments achieve Re much higher than possible in laboratory conditions, many challenges remain. First, it is difficult to obtain stationary, near-neutral data for long periods of time due to variability in wind and temperature conditions in the field, resulting in higher estimated statistical convergence errors. To highlight this issue, the sampling periods needed to achieve < 5% error from lack of statistical convergence for the current dataset is presented in Table 4 for $p = 1$ and $p = 2$. The sampling times are expected to increase for higher-order moments. There is also uncertainty in the boundary layer height $\delta = 60$ m, which is estimated by comparing the $\overline{u'^2}$ profiles with the relation proposed by Marusic and Kunkel (2003). This would contribute to a shift in the values of the integrated parameters, namely the relative amount of energy contributing to $A_{1,\theta'}$ and $B_{1,\theta'}$. Similarly, u_* and θ_* values are estimated from a nearby but not collocated sonic anemometer, and the assumption of a constant flux layer also lend uncertainties to the results. Huang and Katul (2022) discuss these issues in further detail.

Although the bulk of the measured temperature statistics are near-Gaussian, the tails exhibit slightly super-Gaussian behavior with skewness factors ranging from 0.06 to 0.29 and flatness factors from 2.98 to

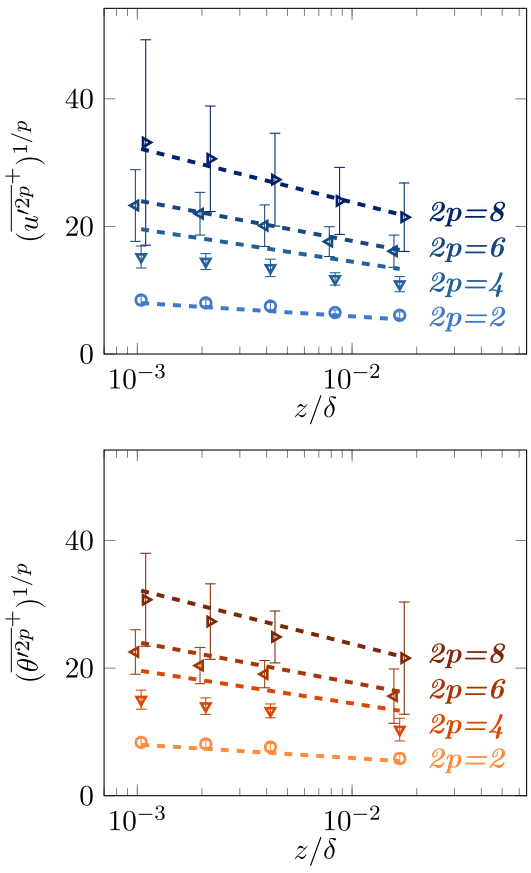

Fig. 7. Profiles of high-order moments of velocity (top) and temperature (bottom) as a function of normalized distance from the ground z/δ. Central moments for $2p$ = 2, 4, 6, and 8 are denoted by (∘), (▽), (◁), and (▷) symbols, respectively. The dashed lines represent the predictions for high-order moments as computed using Eq. (1) for the velocity statistics (Katul et al., 2016) and Eq. (9) for the temperature statistics. High-moments for velocity (blue) and temperature (orange) are denoted with darker shades of their respective colors. Error bars indicate errors due to limited statistical convergence of high-order moments of signal s, calculated as $err^2_{\overline{s'^n}} = \frac{2\mathcal{L}_T}{T_{test}}\left(\frac{\overline{s'^{2n}} - \overline{s'^n}^2}{\overline{s'^n}^2}\right)$, where $\mathcal{L}_T$ is the integral time scale and T_{test} = 30 min is the total sampling period. (For interpretation of the references to color in this figure legend, the reader is referred to the web version of this article.)

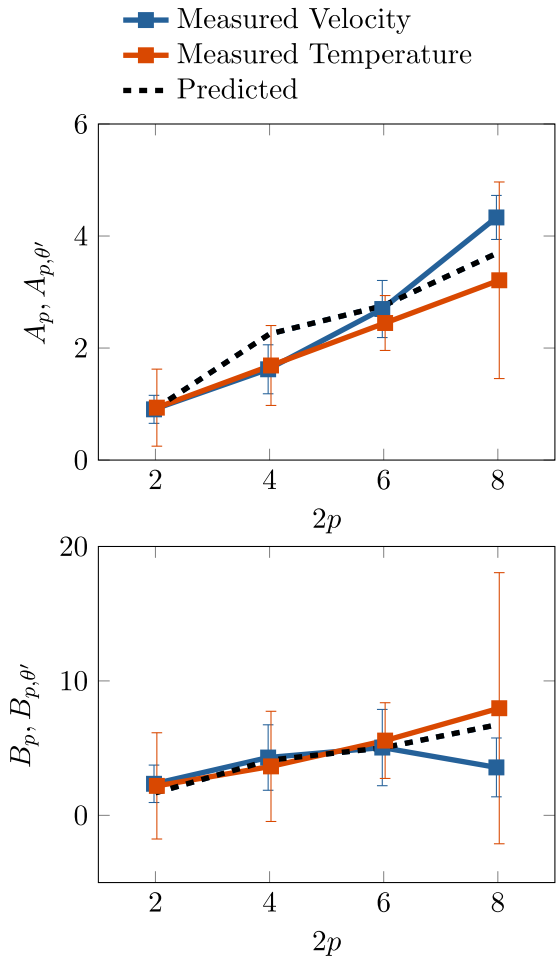

Fig. 8. Coefficients A_p and $A_{p,\theta'}$ (top) and B_p and $B_{p,\theta'}$ (bottom) and as a function of moment order $2p$, averaged across available datasets. Square markers (□) denote slopes (A_p and $A_{p,\theta'}$) and offsets (B_p and $B_{p,\theta'}$) determined through a linear regression of the central moment profiles for $2p$ = 2, 4, 6, and 8. Error bars represent a 95% confidence interval on the regression coefficients from fitting estimator values. The dashed lines represent the coefficients as predicted by integration of the spectral model and RSDH predictions given by Eqs. (1) and (9). Due to their similarity, these RSDH predictions appear overlapping.

3.23. As discussed in the Results section, the lowest measurement station exhibited the highest skewness and flatness factors, which could be indicative of roughness sublayer effects. Deviations from the Gaussian assumption could affect the scaling coefficient $\alpha(p)$ as given in Eq. (4), which is derived from Gaussian statistics.

An additional contribution to the discrepancies that arise in the theoretical results can be explained by the nature of Eq. (4), which was derived by Van Atta and Wyngaard (1975) under the assumption that the higher wavenumbers in the spectrum $E(k)$ followed a $k^{-5/3}$ model proposed by von Kármán and discussed by Hinze (1959). The integration of this model assumed large wavenumbers and considered only the leading term in a convolution following an asymptotic expansion. The resulting expression is Eq. (4), which has explicitly not treated the low wavenumbers, including the k^{-1} region. As this model breaks down for wavenumbers on the order of the Taylor micro-scale, the lower wavenumber regions should depart from the theoretical inertial range behavior. This deviation is evident in Fig. 9, which compares the actual higher-order temperature spectrum ($p \geq 2$, in color) with the theoretical spectrum from the RSDH (shown in gray). The deviation between actual and calculated can be seen to be exacerbated for the lower wavenumber region, with the location of the Taylor micro-scale indicated by the vertical dashed lines. This results in the RSDH over-predicting the higher-order spectrum throughout the datasets. This behavior is consistent with Huang and Katul (2022), which demonstrated the RSDH over-predicted the higher-order velocity spectra. However, the hard truncation of the spectral model at the Batchelor scale, the assumed Saffman spectrum in the lowest k region, and the piecewise discontinuities between each region will likely mean a loss in energy from the RSDH, which may compensate for the over-prediction in the large wavenumbers.

Although statistical similarities between streamwise velocity and passive scalar fluctuations in isotropic or wall-bounded turbulence have been established in multiple studies (see the Background section), the logarithmic law for mean temperature seems to fail away from the wall and in flows whose velocity field changes rapidly (Bradshaw and Huang, 1995). Similarly, while a k^{-1} region is predicted for the streamwise velocity component by the attached eddy hypothesis, such a spectral feature has had far less substantiation for the temperature

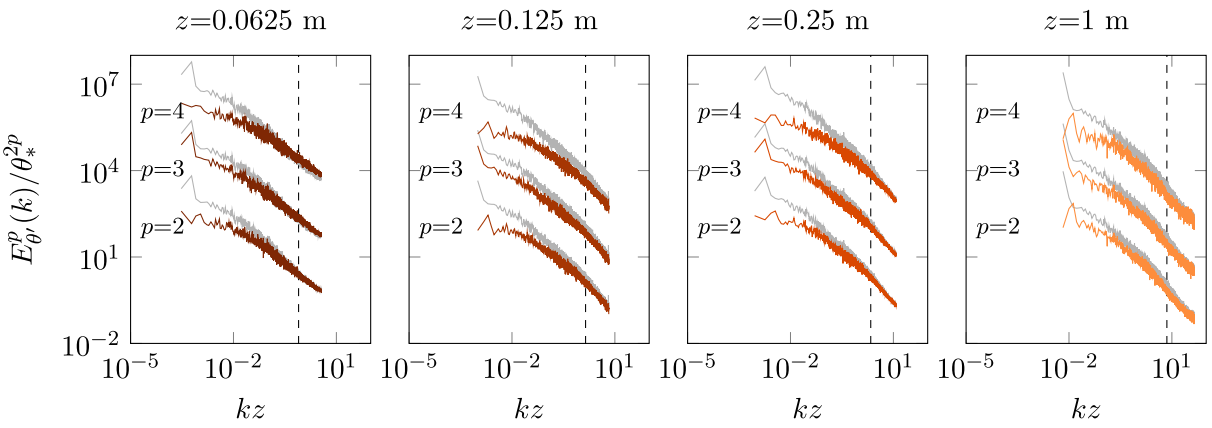

Fig. 9. Calculated higher-order spectra ($p \geq 2$), shown in color, compared with the theoretical spectra from the RSDH, shown in gray, for each measurement location. Dashed black lines indicate $kz = z/\lambda$, where λ is the Taylor micro-scale. (For interpretation of the references to color in this figure legend, the reader is referred to the web version of this article.)

Table 4
Sampling periods (min) needed to achieve a variability of 5% for moment orders $p = 1$ and $p = 2$.

z (m)	u'		θ'	
	$p = 1$	$p = 2$	$p = 1$	$p = 2$
0.0625	65	357	72	396
0.125	43	234	83	455
0.25	66	361	73	401
0.5	41	224	–	–
1.0	86	471	211	1162

fluctuations. Nonetheless, k^{-1} spectral scaling has been encountered in high Re flows, such as the atmospheric boundary layer (Li et al., 2016 and references therein), including the data obtained for the present analysis. The current measurements suggest that for the experimental conditions, there is both a logarithmic region in the mean temperature and sufficient scale separation for the k^{-1} spectral feature in the temperature spectra. The assertion of statistical similarity between temperature and velocity is an ansatz informed by the current dataset and observations of DNS studies, and requires further investigation to establish the conditions under which these assumptions are valid.

6. Conclusions

The similarity between temperature and momentum is used to propose a new theory for the behavior of passive scalar moments in the inertial sublayer based on RSDH. The predicted behavior from the new model is found to be in good agreement with highly resolved measurements of temperature obtained in the atmospheric surface layer under near-neutral conditions with deviations smaller from RSDH behavior than their collocated streamwise velocity counterpart. One potential explanation for the higher deviation in the velocity moments is the non-locality of pressure acting on the velocity components, which is not present in the temperature field. Additionally, the ideal spectrum selected is continuous but not smooth and has a hard transition from inertial to viscous wavenumbers at the Batchelor scale. These, coupled with the multiplicative factor of $\alpha(p)$ in Eq. (4), can combine to have competing effects of under-predicting and over-predicting the spectral energy, respectively. While the performance of the new model is encouraging, extending and evaluating this framework under non-neutral stability conditions and turbulent $Pr \neq 1$ remains an area of future investigation.

CRediT authorship contribution statement

Kelly Y. Huang: Conceptualization, Methodology, Formal analysis, Investigation, Data processing, Writing – original draft, Writing – review & editing. **Matt K. Fu:** Investigation, Writing – original draft, Writing – review & editing, Visualization. **Clayton P. Byers:** Investigation, Writing – original draft, Writing – review & editing, Visualization. **Andrew D. Bragg:** Validation, Writing – review & editing. **Gabriel G. Katul:** Conceptualization, Methodology, Writing – review & editing.

Declaration of competing interest

The authors declare that they have no known competing financial interests or personal relationships that could have appeared to influence the work reported in this paper.

Data availability

Data will be made available on request.

Acknowledgments

GGK acknowledges support from the U.S. National Science Foundation (NSF-AGS-2028633) and the Department of Energy (DE-SC0022072), KYH from ONR Grant No. N00014-21-1-2296 (Fatima Multidisciplinary University Research Initiative) administered by the Marine Meteorology and Space Program of the Office of Naval Research, and ADB from the U.S. National Science Foundation (NSF-CBET-2042346).

Appendix. Boundary layer parameters

The number of eddy turnovers in the datasets are calculated in two different ways. An estimate of the number large scale eddy turnovers, $N_e = T_{test}/(\delta/\bar{u})$, with T_{test} the total dataset time, δ the boundary layer height, and $\bar{u}$ the mean velocity, for each of the four main datasets ranges from $196 \leq N_e \leq 226$ for the four datasets. The mean velocity is taken at $z = 2$ m, which provides a significant underestimate of the large scale eddy turnover time.

The local calculation for eddy turnovers, N_{le}, at each measurement station height is shown in Table A.5, with $N_{le} = T_{test}/\mathcal{L}_T$ and $\mathcal{L}_T$ is the integral time scale calculated from the autocorrelation of the velocity data. This shows that each station has at least 500 local eddy turnovers.

Table A.5
Estimate of eddy turnover times for each sensor location.

z (m)	$T_{test}/\mathcal{L}_T$
0.0625	739.6
0.125	1129
0.25	1180
1.0	560.4

References

Arwatz, G., Fan, Y., Bahri, C., Hultmark, M., 2015. Development and characterization of a nano-scale temperature sensor (T-NSTAP) for turbulent temperature measurements. Meas. Sci. Technol. 26 (3), 035103.

Bendat, J.S., Piersol, A.G., 2011. Random Data: Analysis and Measurement Procedures. John Wiley & Sons.

Bradshaw, P., Huang, G.P., 1995. The law of the wall in turbulent flow. Proc. R. Soc. London. Ser. A: Math. Phys. Sci. 451 (1941), 165–188.

Castillo, L., Hussain, F., 2017. The logarithmic and power law behaviors of the accelerating, turbulent thermal boundary layer. Phys. Fluids 29 (2), 020718.

Cheng, Y., Li, Q., Li, D., Gentine, P., 2021. Logarithmic profile of temperature in sheared and unstably stratified atmospheric boundary layers. Phys. Rev. Fluids 6 (3), 034606.

Chu, C.R., Parlange, M.B., Katul, G.G., Albertson, J.D., 1996. Probability density functions of turbulent velocity and temperature in the atmospheric surface layer. Water Resour. Res. 32 (6), 1681–1688.

Corrsin, S., 1951. On the spectrum of isotropic temperature fluctuations in an isotropic turbulence. J. Appl. Phys. 22 (4), 469. http://dx.doi.org/10.1063/1.1699986.

Fan, Y., Arwatz, G., Van Buren, T.W., Hoffman, D.E., Hultmark, M., 2015. Nanoscale sensing devices for turbulence measurements. Exp. Fluids 56 (7), 138.

Guezennec, Y., Stretch, D., Kim, J., 1990. The structure of turbulent channel flow with passive scalar transport. In: Studying Turbulence using Numerical Simulation Databases. 3: Proceedings of the 1990 Summer Program. pp. 127–138.

Heisel, M., Katul, G.G., Chamecki, M., Guala, M., 2020. Velocity asymmetry and turbulent transport closure in smooth-and rough-wall boundary layers. Phys. Rev. Fluids 5 (10), 104605.

Hinze, J.O., 1959. Turbulence: An Introduction to Its Mechanisms and Theory. McGraw-Hill.

Huang, K.Y., Brunner, C.E., Fu, M.K., Kokmanian, K., Morrison, T.J., Perelet, A.O., Calaf, M., Pardyjak, E., Hultmark, M., 2021a. Investigation of the atmospheric surface layer using a novel high-resolution sensor array. Exp. Fluids 62 (4), 1–13.

Huang, K.Y., Katul, G.G., 2022. Profiles of high-order moments of longitudinal velocity explained by the random sweeping decorrelation hypothesis. Phys. Rev. Fluids 7 (4), 044603. http://dx.doi.org/10.1103/PhysRevFluids.7.044603.

Huang, K.Y., Katul, G.G., Hultmark, M., 2021b. Velocity and temperature dissimilarity in the surface layer uncovered by the telegraph approximation. Bound.-Lay. Meteorol. 180 (3), 385–405.

Hultmark, M., Ashok, A., Smits, A.J., 2011. A new criterion for end-conduction effects in hot-wire anemometry. Meas. Sci. Technol. 22 (5), 055401. http://dx.doi.org/10.1088/0957-0233/22/5/055401.

Hutchins, N., Chauhan, K., Marusic, I., Monty, J., Klewicki, J., 2012. Towards reconciling the large-scale structure of turbulent boundary layers in the atmosphere and laboratory. Bound.-Lay. Meteorol. 145 (2), 273–306.

Kader, B.A., 1981. Temperature and concentration profiles in fully turbulent boundary layers. Int. J. Heat Mass Transfer 24 (9), 1541–1544. http://dx.doi.org/10.1016/0017-9310(81)90220-9.

Kader, B., Yaglom, A., 1972. Heat and mass transfer laws for fully turbulent wall flows. Int. J. Heat Mass Transfer 15 (12), 2329–2351.

Kasagi, N., Tomita, Y., Kuroda, A., 1992. Direct numerical simulation of passive scalar field in a turbulent channel flow. J. Heat Transfer 114 (3), 598–606.

Katul, G.G., Banerjee, T., Cava, D., Germano, M., Porporato, A., 2016. Generalized logarithmic scaling for high-order moments of the longitudinal velocity component explained by the random sweeping decorrelation hypothesis. Phys. Fluids 28 (9), 095104.

Katul, G.G., Chu, C.R., Parlange, M.B., Albertson, J.D., Ortenburger, T.A., 1995. Low-wavenumber spectral characteristics of velocity and temperature in the atmospheric surface layer. J. Geophys. Res.: Atmos. 100 (D7), 14243–14255.

Kays, W.M., 1994. Turbulent Prandtl number. Where are we? ASME J. Heat Transf. 116 (2), 284–295.

Kim, J., Moin, P., 1987. Transport of passive scalars in a turbulent channel flow. In: Sixth Symposium on Turbulent Sheet Flows. NASA, pp. 85–96.

Klewicki, J.C., Foss, J.F., Wallace, J.M., 1998. High Reynolds number [R_θ=o(10^6)] boundary layer turbulence in the atmospheric surface layer above western Utah's salt flats. In: Flow At Ultra-High Reynolds and Rayleigh Numbers. Springer, pp. 450–466.

Kolmogorov, A.N., 1941. The local structure of turbulence in incompressible viscous fluid for very large Reynolds numbers. Cr Acad. Sci. URSS 30, 301–305.

Li, D., Katul, G.G., Gentine, P., 2016. The k- 1 scaling of air temperature spectra in atmospheric surface layer flows. Q. J. R. Meteorol. Soc. 142 (694), 496–505.

Lohse, D., 1994. Temperature spectra in shear flow and thermal convection. Phys. Lett. A 196 (1–2), 70–75. http://dx.doi.org/10.1016/0375-9601(94)91046-4, arXiv:9408003.

Marusic, I., Kunkel, G.J., 2003. Streamwise turbulence intensity formulation for flat-plate boundary layers. Phys. Fluids 15 (8), 2461–2464.

Marusic, I., Monty, J., Hultmark, M., Smits, A., 2013. On the logarithmic region in wall turbulence. J. Fluid Mech. 716, R3. http://dx.doi.org/10.1017/jfm.2012.511.

Meneveau, C., Marusic, I., 2013. Generalized logarithmic law for high-order moments in turbulent boundary layers. J. Fluid Mech. 719, R1. http://dx.doi.org/10.1017/jfm.2013.61.

Metzger, M.M., Klewicki, J.C., 2001. A comparative study of near-wall turbulence in high and low Reynolds number boundary layers. Phys. Fluids 13 (3), 692–701.

Morales, A., Wächter, M., Peinke, J., 2012. Characterization of wind turbulence by higher-order statistics. Wind Energy 15 (3), 391–406.

Morrison, T., Calaf, M., Higgins, C.W., Drake, S.A., Perelet, A., Pardyjak, E., 2021. The impact of surface temperature heterogeneity on near-surface heat transport. Bound.-Lay. Meteorol. 180 (2), 247–272.

Obukhov, A., 1949. Temperature field structure in a turbulent flow. Izv. Acad. Nauk SSSR Ser. Geog. Geofiz 13, 58–69.

Overholt, M.R., Pope, S.B., 1996. Direct numerical simulation of a passive scalar with imposed mean gradient in isotropic turbulence. Phys. Fluids 8 (11), 3128. http://dx.doi.org/10.1063/1.869099.

Pirozzoli, S., Bernardini, M., Orlandi, P., 2016. Passive scalars in turbulent channel flow at high Reynolds number. J. Fluid Mech. 788, 614–639.

Pond, S., Smith, S., Hamblin, P., Burling, R., 1966. Spectra of velocity and temperature fluctuations in the atmospheric boundary layer over the sea. J. Atmos. Sci. 23 (4), 376–386.

Saffman, P.G., 1967. The large-scale structure of homogeneous turbulence. J. Fluid Mech. 27 (3), 581–593. http://dx.doi.org/10.1017/S0022112067000552.

Samie, M., Marusic, I., Hutchins, N., Fu, M.K., Fan, Y., Hultmark, M., Smits, A.J., 2018. Fully resolved measurements of turbulent boundary layer flows up to Re_τ=20,000. J. Fluid Mech. 851, 391–415. http://dx.doi.org/10.1017/jfm.2018.508.

Smits, A.J., McKeon, B.J., Marusic, I., 2011. High–Reynolds number wall turbulence. Annu. Rev. Fluid Mech. 43 (1), 353–375. http://dx.doi.org/10.1146/annurev-fluid-122109-160753.

Sreenivasan, K.R., 1991. On local isotropy of passive scalars in turbulent shear flows. Proc. R. Soc. London. Ser. A: Math. Phys. Sci. 434 (1890), 165–182.

Stevens, R.J., Wilczek, M., Meneveau, C., 2014. Large-eddy simulation study of the logarithmic law for second-and higher-order moments in turbulent wall-bounded flow. J. Fluid Mech. 757, 888–907.

Subramanian, C., Antonia, R., 1981. Effect of Reynolds number on a slightly heated turbulent boundary layer. Int. J. Heat Mass Transfer 24 (11), 1833–1846.

Taylor, G.I., 1938. The spectrum of turbulence. Proc. R. Soc. London. Ser. A-Math. Phys. Sci. 164 (919), 476–490.

Tennekes, H., 1975. Eulerian and Lagrangian time microscales in isotropic turbulence. J. Fluid Mech. 67 (3), 561–567.

Tennekes, H., Lumley, J.L., 1972. A First Course in Turbulence. MIT Press.

Townsend, A., 1976. The Structure of Turbulent Shear Flow. Cambridge University Press.

Vallikivi, M., Hultmark, M., Smits, A.J., 2015. Turbulent boundary layer statistics at very high Reynolds number. J. Fluid Mech. 779, 371–389. http://dx.doi.org/10.1017/jfm.2015.273.

Van Atta, C., Wyngaard, J., 1975. On higher-order spectra of turbulence. J. Fluid Mech. 72 (4), 673–694.

Warhaft, Z., 2000. Passive scalars in turbulent flows. Annu. Rev. Fluid Mech. 32 (1), 203–240. http://dx.doi.org/10.1146/annurev.fluid.32.1.203.

Wei, T., Fife, P., Klewicki, J., McMurtry, P., 2005. Properties of the mean momentum balance in turbulent boundary layer, pipe and channel flows. J. Fluid Mech. 522, 303–327.

Wu, X., Moin, P., 2010. Transitional and turbulent boundary layer with heat transfer. Phys. Fluids 22 (8), 085105.

Yang, X.I.A., Abkar, M., 2018. A hierarchical random additive model for passive scalars in wall-bounded flows at high Reynolds numbers. J. Fluid Mech. 842, 354–380. http://dx.doi.org/10.1017/jfm.2018.139.

Yeung, P.K., Sawford, B.L., 2002. Random-sweeping hypothesis for passive scalars in isotropic turbulence. J. Fluid Mech. 459, 129–138. http://dx.doi.org/10.1017/S0022112002008248.